Accepted Manuscript

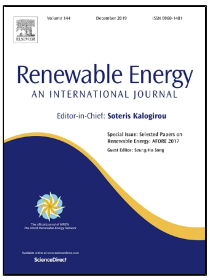

Flexible Dynamic Modeling and Analysis of Drive Train for Offshore Floating Wind Turbine

Zhanwei Li, Binrong Wen, Kexiang Wei, Wenxian Yang, Zhike Peng, Wenming Zhang

PII:	S0960-1481(19)30950-4
DOI:	10.1016/j.renene.2019.06.116
Reference:	RENE 11848
To appear in:	*Renewable Energy*
Received Date:	07 September 2018
Accepted Date:	20 June 2019

Please cite this article as: Zhanwei Li, Binrong Wen, Kexiang Wei, Wenxian Yang, Zhike Peng, Wenming Zhang, Flexible Dynamic Modeling and Analysis of Drive Train for Offshore Floating Wind Turbine, *Renewable Energy* (2019), doi: 10.1016/j.renene.2019.06.116

Flexible Dynamic Modeling and Analysis of Drive Train for Offshore Floating Wind Turbine

Zhanwei Li[1], Binrong Wen[1], Kexiang Wei[2], Wenxian Yang[3], Zhike Peng[1]*, Wenming Zhang[1]

1. *State Key Laboratory of Mechanical System and Vibration*, *Shanghai Jiao Tong University, Shanghai, China, 200240;*

2. *Hunan Provincial Engineering Laboratory of Wind Power Operation, Maintenance and Testing, Hunan Institute of Engineering, Xiangtan, China, 411104;*

3. *School of Marine Science and Technology, Newcastle University, Newcastle upon Tyne, UK NE1 7RU;*

Abstract

Drive train has a significant influence on the reliability of wind turbines. As for the Offshore Floating Wind Turbine (OFWT), the importance of the drive train is even more prominent due to the more complex operating conditions at the ocean. In this study, dynamic characteristics of the OFWT drive train are investigated based on flexible dynamic model. First, this paper presents a flexible dynamic model of the drive train, which includes not only the full coupling of gear meshing but also the flexibilities of planet carrier and ring gear. Then, a corresponding finite element model is established to verify the reliability of the proposed model by comparing natural frequencies and vibration responses. Afterwards, dynamic characteristics of the drive train are analyzed under different excitations, including the time-varying mesh stiffness, wind turbulence, tower shadow, wind shear and platform motions. Results show that resonant peaks of the system are more likely to appear when the mesh frequency or its multiplication of the gear pair 1-2 is equal to the natural frequency. In addition, it is revealed that the tower shadow is the most significant excitation source for OFWT drive train, followed by platform pitch and surge motions.

Keywords: Offshore Floating Wind Turbine; drive train; flexible dynamic model; dynamic characteristics

* Corresponding author.

E-mail address: z.peng@sjtu.edu.cn (Z. Peng).

1. Introduction

Wind energy is clean and renewable. As there are fewer and fewer economically exploitable wind resources on land, the construction of wind farms are being exploited from land to ocean. The Offshore Floating Wind Turbine (OFWT) is subjected to more complex operating conditions than bottom fixed wind turbine in land. A reliable and cost-effective driven train is significant for smooth and steady power generation. In addition, better dynamic characteristics of drive train are benefit for enhancing the service life of whole wind turbine [1, 2].

Many dynamic models have been proposed to analyze the dynamic characteristics of the wind turbine driven train. According to the number of Degrees of Freedom (DOFs) and the complexity, the exciting model can be generally classified into three categories: (a) Purely torsional rigid multibody models [3-7]; (b) Three-, four- or six-DOF rigid multibody models [8-20]; (c) Flexible multibody models [21-26]. The purely torsional rigid multibody model only takes the torsional rigidities of shafts and gears into consideration. Therefore, it only reveals the twisting vibration of the drive train roughly. Abo-Khalil et al. [3] established a two-mass oscillating system to simulate the mechanical coupling of turbine and generator. Considering the uncertain parameters, Wei et al. [4] simplified the drive train of wind turbine as a one-stage gear pair system. Gu et al. [5] combined the rigid drive train model with the aerodynamic subsystem model and generator subsystem model to generate a full dynamic model of the cage wind turbine. Shi et al. [6] proposed a torsional multibody dynamic model base on Lagrange formulation to investigate the transient responses of drive train. Considering the wind gust and internal excitations of drive train, Zhao et al. [7] analyzed the nonlinear torsional vibrations of a wind turbine gearbox. The three- and four-DOF rigid multibody models take the translational and one rotational DOFs into account. However, the six-DOF rigid multibody models includes the three-dimensional space motion of drive train. Guo et al. [8, 9] proposed a lumped-parameter model under the effect of gravity, in which each rigid body has two translational and one rotational DOFs. Similarly, Shi et al. [10] and Srikanth et al. [11, 12] also established a

three-DOF multibody model, in which the gear shafts were modeled as torsional springs. Based on the Lagrange formulation, Qin et al. [13], Yi et al. [14], Zhao et al. [15] and Zhai et al. [16] established a four-DOF multibody rigid dynamic model of drive train, which includes the three translational and one rotational DOFs. Considering the effect of the flexible pins, Zhu et al. [17] proposed a three-DOF dynamic model of spur gear drive train. Li et al. [18] presented a simulation framework to investigate wind turbine aero-servo-elastic behavior, in which the shafts and gears were represented by six-DOF rigid bodies in Virtual. Lab. Motion. Nejad et al. [19, 20] established a six-DOF rigid model in SIMPACK software to investigate the correlation between the tower-top axial acceleration and the load effects in drive train. In order to improve the load distribution between the planet gears and reduce the weight of the transmission system, the thickness of the ring gear rim is designed to be thin [27, 28]. Taking the flexibilities of the planet carrier and gearbox housing into account, Helsen et al. [21] investigated the effectiveness of the three different configurations of drive train. Considering the flexibilities of main shaft, planet carrier, gear shafts and gearbox housing, Guo et al. [22] adopted SIMPACK to establish a three-dimensional dynamic model taking the effects of the gravity and bending moments into account. Similarly, Wang et al. [23] and Zhu et al. [24, 25] also established a rigid-flexible coupling model in SIMPACK, in which the flexibilities of planet carrier and gearbox housing were included. Xing et al. [26] modeled the condensed flexible bodies using ABAQUS software and imported them into SIMPACK to establish a flexible dynamic model of drive train. Peeters et al. [29], Helsen et al. [30] and Jin et al. [31] described and discussed the three modeling techniques outlined above, showing that the flexible multibody dynamic model is the most accurate model to reflect the dynamic characteristics of the wind turbine drive train.

Dynamic excitations of the OFWT drive train is diverse due to the complex operating conditions, and they can be classified as the external and internal excitations [24]. The external excitations mainly include the Wind Turbulence (WT), Wind Shear (WS), Tower Shadow (TS) and Platform Motions (PMs). Among all the above mentioned external excitations, PMs are unique for OFWT. The internal excitations mainly consist of the Time-

varying Mesh Stiffness (TVMS), the static translation errors due to the manufacturing errors or gear tooth modifications, assembly errors and other faults of gears and shafts. TVMS is a unique excitation of the gear transmission system, which is widely considered in almost all the papers mentioned above. Srikanth et al. [11] meticulously described the calculation process of aerodynamic torque due to the variation of the wind speed based on Danish standard DS472, then analyzed the dynamic characteristics of drive train under WT. Li et al. [18] and Abo-Khalil et al. [3] analyzed the power fluctuation due to the WT and TS. The axial force and the bending moment at the tower top were analyzed in Ref. [20] under the effects of uncertain wind speed and wave height.

The above mentioned researches show that the torsional multibody model only suits the initial analysis. The three-, four- and six-DOF rigid model may lost some important information about the flexibilities of local components. Hence the flexible model should be used to analyze the dynamic characteristics of drive train for OFWT. Most scholars combined the commercial finite element (FE) software (such as ABAQUS) with multi-body dynamic software (such as SIMPACK) to establish the rigid-flexible models. It is inconvenient and difficult to exchange data in real time with turbine controllers and environmental excitation calculation modules when one wants to construct an integrated simulation framework to analyze the dynamic characteristics of drive train. Secondly, the analyses about the effects of TS and WS are insufficient on the dynamic characteristics of drive train. Many researchers only focus on dynamic characteristics of wind turbine under WT and they often pay more attentions on power fluctuations due to the TS and WS. Thirdly, the OFWT is the development tendency of the wind turbine, but few researchers meticulously analyze the effects of PMs on dynamic characteristics of drive train. This paper mainly focuses on the following aspects:

(1) A flexible dynamic model is established to analyze the dynamic characteristics of the OFWT drive train, in which the flexibilities of the planet carrier, ring gear and gear shafts are considered. Meanwhile, based on ANSYS software, an FE model is established to verify the reliability of the proposed model in this paper.

(2) The dynamic characteristics of OFWT drive train under the excitations of TVMS, WT, TS, WS and PMs

are analyzed in detail.

The frame of this paper can be summarized as follows: after this introduction, in Section 2, a flexible dynamic model of OFWT drive train is established. In Section 3, the proposed model is verified by comparing the natural frequencies and dynamic responses obtained from two models. Afterwards, the effects of TVMS, TS, WS, WT, and PMs on dynamic characteristics of drive train are meticulously analyzed. Conclusions are drawn in Section 4.

2. Modeling of wind turbine drive train

The flexible dynamic model of the drive train is established in this section. A classical wind turbine drive train assembly is shown in Fig. 1a, which includes a low-speed helical planetary gear stage and two helical parallel shaft gear stages. The flexible dynamic model mainly includes two parts: the meshing model of helical gear pairs (including the external meshing and internal meshing) and the flexible model of the planet carrier and ring gear. In Section 2.1, the meshing model of the helical planetary gear (see Fig. 1b) is introduced firstly. The flexible model of planet carrier (see Fig. 1c) and ring gear (see Fig. 1d) is described in Section 2.2 subsequently. Finally, the whole flexible condensed dynamic model of drive train is established in Section 2.3.

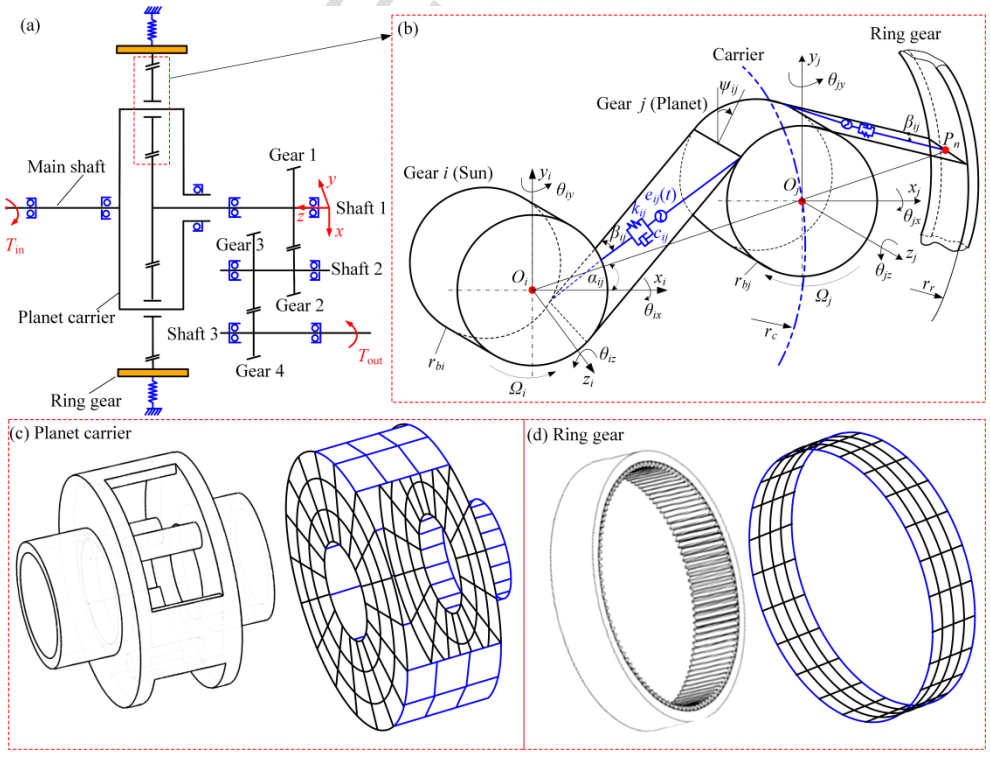

Fig. 1 Schematic of the whole flexible model: (a) drive train assembly; (b) meshing model of the helical planetary gear stage; (c) schematic and discrete model of planet carrier; (d) schematic and discrete model of ring gear

2.1 Meshing model of the helical gear pair

Here taking the helical planetary gear stage as an example, it includes the external meshing and internal meshing gear pairs simultaneously. The meshing model of the helical planetary gear stage is shown in Fig. 1b, in which r_{bi}, r_{bj}, O_i, O_j denote the radii of base circles, geometrical centers of gears i and j. r_c, r_r and β_{ij} denote the radii of the planet carrier, ring gear pitch circle and helix angle, respectively. Sun gear and planet gears are modeled as lumped masses with six-DOF, and they are connected by a liner spring to simulate the gear meshing. External meshing model of the helical gear pair has been given in the previous researches [32, 33], but they ignore the effects of the gear swing in x- and y-direction. In this paper, modification is conducted and the relative displacement of the external meshing gear pair is rewritten as:

$$\begin{aligned} p_{exter}(t) = & [-(x_i - \mathrm{sgn}1\times\mathrm{sgn}2\times\theta_{yi}\times l_1)\sin\psi_{ij} + (x_j + \mathrm{sgn}1\times\mathrm{sgn}2\times\theta_{yj}\times l_2)\sin\psi_{ij} + (y_i + \mathrm{sgn}1\times\mathrm{sgn}2\times \\ & \theta_{xi}\times l_1)\cos\psi_{ij} - (y_j - \mathrm{sgn}1\times\mathrm{sgn}2\times\theta_{xj}\times l_2)\cos\psi_{ij} + \mathrm{sgn}1\times r_{bi}\theta_{zi} + \mathrm{sgn}1\times r_{bj}\theta_{zj}]\cos\beta_{ij} \\ & + [\mathrm{sgn}1\times z_i - \mathrm{sgn}1\times z_j + r_{bi}\sin\psi_{ij}\theta_{xi} + r_{bj}\sin\psi_{ij}\theta_{xj} - r_{bi}\theta_{yi}\cos\psi_{ij} - r_{bj}\theta_{yj}\cos\psi_{ij}]\sin\beta_{ij} - e_{ij}(t) \end{aligned}, \quad (1)$$

where x_i, x_j, y_i, y_j, z_i, z_j, θ_{xi}, θ_{xj}, θ_{yi}, θ_{yj}, θ_{zi}, θ_{zj} denote the displacements in six directions of gear i and gear j. ψ_{ij} is the angle between the plane of action and positive y-axis. It can be expressed as:

$$\psi_{ij} = \begin{cases} -\varphi_{ij} + \alpha_{ij} & \Omega_i:\ \text{Couterclockwise} \\ \varphi_{ij} + \alpha_{ij} - \pi & \Omega_i:\ \text{Clockwise} \end{cases}, \quad (2)$$

where φ_{ij} is the operating pressure angle of gear pairs; α_{ij} is the relative position angle between the connecting line of gear centers and the positive x-axis of gear i. l_1 and l_2 are arms of force due the gear swing in x- and y-direction, which can be calculated as follow:

$$\begin{cases} l_1 = r_{bi}\tan\varphi_{ij}\tan\left|\beta_{ij}\right| \\ l_2 = r_{bj}\tan\varphi_{ij}\tan\left|\beta_{ij}\right| \end{cases}, \quad (3)$$

sgn1 and sgn2 are defined as follows:

$$\mathrm{sgn}1 = \begin{cases} 1 & \Omega_i:\ \text{Couterclockwise} \\ -1 & \Omega_i:\ \text{Clockwise} \end{cases}, \quad \mathrm{sgn}2 = \begin{cases} 1 & \beta_{ij} > 0 \\ -1 & \beta_{ij} < 0 \end{cases}, \quad (4)$$

In this paper, gears are supposed to be healthy and gear tooth are not modified. Therefore, the static transmission

error excitation function $e_{ij}(t)$ is equal to zero all the time in this paper.

For the internal meshing, the liner spring is tangent to the base cylinder of the planet gear and linked to the pitch node (P_n in Fig. 1b) of ring gear. So the relative displacement of the internal gear meshing can be written as:

$$\begin{aligned} p_{inter}(t) = [-(x_i - \mathrm{sgn}1\times\mathrm{sgn}2\times\theta_{yi}\times l_1)\sin\psi_{ij} + (x_j + \mathrm{sgn}1\times\mathrm{sgn}2\times\theta_{yj}\times l_2)\sin\psi_{ij} + (y_i + \\ \mathrm{sgn}1\times\mathrm{sgn}2\times\theta_{xi}\times l_1)\cos\psi_{ij} - (y_j - \mathrm{sgn}1\times\mathrm{sgn}2\times\theta_{xj}\times l_2)\cos\psi_{ij} + \mathrm{sgn}1\times r_{bi}\theta_{zi}]\cos\beta_{ij}, \\ + [\mathrm{sgn}1\times z_i - \mathrm{sgn}1\times z_j + r_{bi}\sin\psi_{ij}\theta_{xi} - r_{bi}\theta_{yi}\cos\psi_{ij}]\sin\beta_{ij} - e_{ij}(t) \end{aligned} \tag{5}$$

As a result, motion equations of the external and internal meshing helical gear pairs considering the lateral, torsional, axial, and swing coupling are summarized as follow:

$$\boldsymbol{M}_{ij}\ddot{\boldsymbol{X}}_{ij} + \boldsymbol{C}_{ij}\dot{\boldsymbol{X}}_{ij} + \boldsymbol{K}_{ij}\boldsymbol{X}_{ij} = \boldsymbol{F}_{ij}, \tag{6}$$

where $\boldsymbol{M}_{ij}$, $\boldsymbol{C}_{ij}$ and $\boldsymbol{X}_{ij}$ denote the mass matrix, damping matrix and displacement vector matrix of the gear pair *ij*, and they are described particularly in the Refs. [32, 33]. $\boldsymbol{K}_{ij}$ denotes the mesh stiffness matrix of gear pair *ij*, which can be expressed as follow:

$$\boldsymbol{K}_{ij} = k_{ij}\boldsymbol{\alpha}_{ij}^{\mathrm{T}}\cdot\boldsymbol{\alpha}_{ij}, \tag{7}$$

where k_{ij} is the TVMS of the helical gear pair, and $\boldsymbol{\alpha}_{ij}$ can be written as follow:

$$\boldsymbol{\alpha}_{ij} = \begin{cases} [-\sin\psi_{ij}\cos\beta_{ij}, \cos\psi_{ij}\cos\beta_{ij}, \mathrm{sgn}1\times\sin\beta_{ij}, r_{bi}\sin\psi_{ij}\sin\beta_{ij} + \mathrm{sgn}1\times\mathrm{sgn}2\times l_1\cos\beta_{ij}\cos\psi_{ij}, \\ -r_{bi}\cos\psi_{ij}\sin\beta_{ij} + \mathrm{sgn}1\times\mathrm{sgn}2\times l_1\cos\beta_{ij}\sin\psi_{ij}, \mathrm{sgn}1\times r_{bi}\cos\beta_{ij}, \\ \sin\psi_{ij}\cos\beta_{ij}, -\cos\psi_{ij}\cos\beta_{ij}, -\mathrm{sgn}1\times\sin\beta_{ij}, r_{bj}\sin\psi_{ij}\sin\beta_{ij} + \mathrm{sgn}1\times\mathrm{sgn}2\times l_2\cos\beta_{ij}\cos\psi_{ij}, & \text{Extrnal meshing} \\ -r_{bj}\cos\psi_{ij}\sin\beta_{ij} + \mathrm{sgn}1\times\mathrm{sgn}2\times l_2\cos\beta_{ij}\sin\psi_{ij}, \mathrm{sgn}1\times r_{bj}\cos\beta_{ij}] & \\ [-\sin\psi_{ij}\cos\beta_{ij}, \cos\psi_{ij}\cos\beta_{ij}, \mathrm{sgn}1\times\sin\beta_{ij}, r_{bi}\sin\psi_{ij}\sin\beta_{ij} + \mathrm{sgn}1\times\mathrm{sgn}2\times l_1\cos\beta_{ij}\cos\psi_{ij}, & \\ -r_{bi}\cos\psi_{ij}\sin\beta_{ij} + \mathrm{sgn}1\times\mathrm{sgn}2\times l_1\cos\beta_{ij}\sin\psi_{ij}, \mathrm{sgn}1\times r_{bi}\cos\beta_{ij}, & \text{Internal meshing} \\ \sin\psi_{ij}\cos\beta_{ij}, -\cos\psi_{ij}\cos\beta_{ij}, -\mathrm{sgn}1\times\sin\beta_{ij}, 0, 0, 0] & \end{cases}, \tag{8}$$

2.2 Flexible models of the planet carrier and ring gear

Configurations of the planet carrier and the ring gear in this paper are similar to the model in Ref. [34] (see Figs. 1c and 1d). They are complex and difficult to establish adopting the pure analytical method. Therefore, the FE method based on MATLAB is adopted considering the convenience and universality. In order to balance the accuracy and efficiency, an eight-node six-DOF degenerated shell element is adopted (see Fig. 2). The element stiffness and mass stiffness in the global coordinate can be calculated as follows [35]:

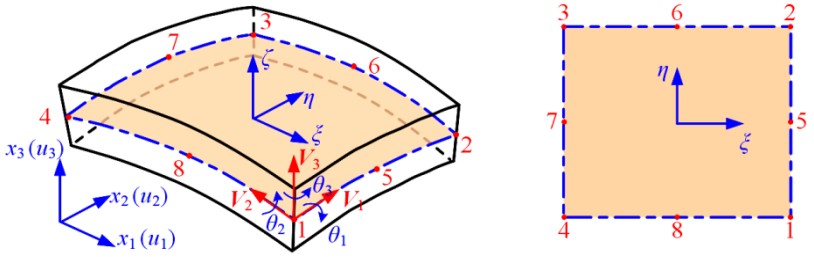

Fig. 2 Eight-node six-DOF degenerated shell element

A generic point position vector of the shell element can be defined according to the position vectors of nodes and shape functions:

$$x_i(\xi,\eta,\zeta)=\sum_{k=1}^{n}N^k(\xi,\eta)x_i^k+\sum_{k=1}^{n}N^k(\xi,\eta)H^k(\zeta)V_{3i}^k \quad (i=1,2,3), \tag{9}$$

where $N^k(\xi,\eta)$, x_i^k, $H^k(\zeta)$ and V_{3i}^k denote the shape functions of the shell in the middle surface, position vectors of the node k, one-dimensional shape function in ζ-direction and the unit vector at node k.

The displacement of a generic point in the shell element can be described as:

$$u_i(\xi,\eta,\zeta)=\sum_{k=1}^{n}N^k(\xi,\eta)u_i^k+\sum_{k=1}^{n}N^k(\xi,\eta)H^k(\zeta)(-V_{2i}^k\theta_1^k+V_{1i}^k\theta_2^k) \quad (i=1,2,3), \tag{10}$$

where u_i^k, V_{1i}^k, V_{2i}^k, θ_1^k and θ_2^k denote the nodal displacement, unit vectors along the reference surface, rotational DOFs along the unit vectors at node k (see Fig. 2) , respectivley. The strain components in six direction can be computed from Eq. (10) by taking the derivative with respect to the x_i-axis.

The strain-displacement relation and the stress-strain relation can be written as:

$$\boldsymbol{\varepsilon}=\boldsymbol{B}\boldsymbol{d},\ \boldsymbol{\sigma}=\boldsymbol{D}\boldsymbol{\varepsilon}, \tag{11}$$

where $\boldsymbol{d}$ is the displacement vector of all nodes; $\boldsymbol{D}$ is the material property matrix; $\boldsymbol{B}$ is the relation matrix of strain-displacement due to the derivative of Eq. (9), and the detailed expression can be found in Ref. [35].

Finally, the element stiffness matrix and the mass matrix can be written as:

$$\begin{aligned}\boldsymbol{K}&=\int_{\Omega^e}\boldsymbol{B}^T\boldsymbol{D}\boldsymbol{B}d\Omega\\ \boldsymbol{M}&=\int_{\Omega^e}\rho\boldsymbol{N}^T\boldsymbol{N}d\Omega\end{aligned}, \tag{12}$$

where ρ is the density of the shell element and the shape function matrix $\boldsymbol{N}$ can be found in Ref. [35]. However, the rotational DOFs are still in terms of local vectors and should be converted to the global axes. Afterwards, the

calculated element stiffness and mass matrixes are assembled into the whole construction matrix by matching the node numbers of elements with each other.

Finally, flexible models of the planet carrier and ring gear are established using the degenerated shell element based on MATLAB (see Fig. 1c and 1d). It is worth noting that the left-portion of the planet carrier is not established using shell elements. This is because that it is connected directly with main shaft using interference fit and replaced by beam elements in this paper. The number of the flexible model DOFs is relatively large, so the Component Mode Synthesis (CMS) method [36] is adopted to reduce the computational consuming in this paper.

2.3 Overall condensed system model of the drive train

Flow chart of the condensed system model analyses of the drive train is shown in Fig. 3. In this paper, the flexibilities of main shaft and the gear shafts are also considered, which are simulated using Timoshenko beams [33]. Gear shafts, the condensed flexible model of planet carrier and the ring gear are linked to each other by gear meshing. Afterwards, they are assembled to produce the overall system flexible model of the drive train according to the FE method. Subsequently, the overall system flexible dynamic model is established using the CMS technology to further improve the solution efficiency. It is worth noting that the nodes of gears and bearings are retained as the external nodes of the condensed system model for considering the excitations of TVMS and PMs. Similarly, the nodes applied in the aerodynamic torque and electromagnetic torque are also retained. Finally, the motion equation of the entire system can be written as follow:

$$\boldsymbol{M}\ddot{\boldsymbol{u}} + \boldsymbol{C}\dot{\boldsymbol{u}} + \boldsymbol{K}\boldsymbol{u} = \boldsymbol{F}_{\boldsymbol{u}}, \tag{13}$$

where $\boldsymbol{M}$, $\boldsymbol{C}$, $\boldsymbol{K}$ and $\boldsymbol{F}_{\boldsymbol{u}}$ denote the mass matrix, damping matrix, stiffness matrix and external force vectors of the system. In this paper, the Rayleigh-type damping and the numerical integration Newmark-β are applied to calculate the dynamic responses of the condensed flexible dynamic model for OFWT drive train. Because the rotor speed of main shaft is low, the rotation effects are negligible and ignored in this study.

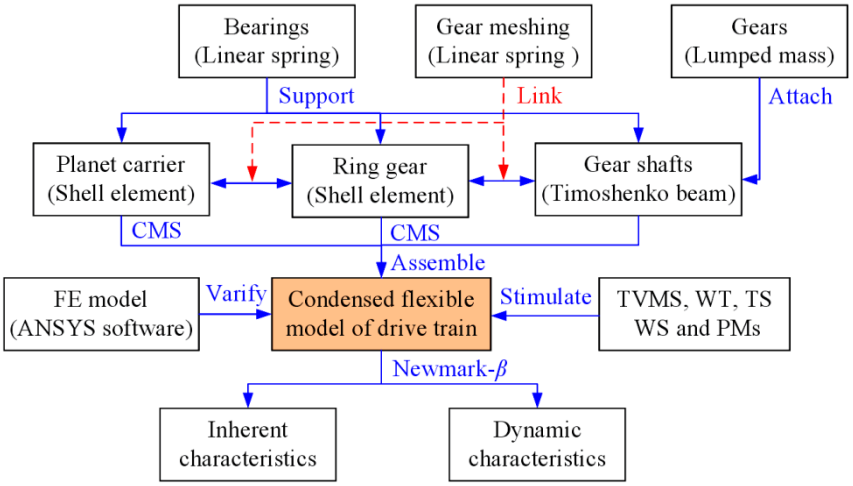

Fig. 3 Flow chart of the condensed flexible model analyses of the drive train

3. Model verification and discussion

In this section, the drive train of a 1.5 WM OFWT is established based on the flexible dynamic modeling method proposed in this paper. The reliability of the proposed model is verified by comparing the natural frequencies and dynamic responses obtained from two models. In addition, the effects of the TVMS, WT, TS, WS and PMs on dynamic characteristics of wind turbine drive train are discussed meticulously base on the proposed model.

3.1 Model verification

The main parameters of the drive train analyzed in this paper are listed in Table 1, and the FE model based on ANSYS software is shown in Fig. 4. The planet carrier and ring gear are simulated using Shell 281 elements; The main shaft and gear shafts are simulated using Beam 188 elements; Gears, gear meshing and bearings are simulated using Mass 21, Combin 14 and Matrix 27 elements, respectively. Because gears are assumed as the rigid disks, a rigid region is established between the gear and the end of the spring element considering the effects of gear swings and rotation. In addition, the “rmodif” command is adopted to simulate the TVMS excitation under transient solution in ANSYS.

Table 1 Main parameters of the drive train

	Low speed			Medium speed		High speed	
Gear name	Sun gear	Planet gear	Ring gear	Gear 1	Gear 2	Gear 3	Gear 4
Tooth number	27	48	123	104	23	98	25
Module (mm)		12		10		6.5	
Width (mm)		300		300		200	
Helix angle (°)		20°		20°		20°	
Direction	Left	Right	Right	Left	Right	Right	Left
Mass (kg)	239.77	306.11	—	1096.04	101.7	189.5	25.87
I (kg·m^2)	2.12	4.96	—	76.08	0.345	4.25	0.035
J (kg·m^2)	4.24	9.92	—	152.16	0.69	8.5	0.07
Ave-mesh stiffness	6.38e9		7.84e9	6.35e9		4.40e9	

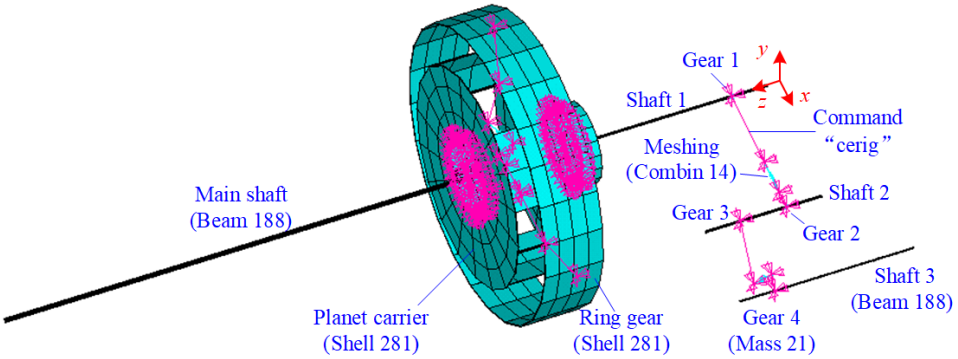

Fig. 4 FE model of the drive train based on ANSYS software

The first 12 orders of natural frequencies of the drive train calculated by the proposed model and the FE model established in ANSYS software are compared in the Table 2. It is observed that the frequencies obtained from the proposed model agree well with those obtained from the FE model, and the maximal relative error is merely 0.62%.

Table 2 Natural frequencies of the drive train

Mode No.	Natural frequencies (Hz)		Relative errors (%)
	Proposed model	FE model	
f_{n1}	95.74	95.73	0.001
f_{n2}	112.87	113.09	0.20
f_{n3}	113.64	113.87	0.21
f_{n4}	123.67	123.83	0.13
f_{n5}	133.96	134.21	0.19
f_{n6}	135.42	135.62	0.16
f_{n7}	142.66	142.64	-0.001
f_{n8}	173.80	173.77	-0.02
f_{n9}	188.53	188.49	-0.02
f_{n10}	195.69	196.68	0.51
f_{n11}	200.53	201.76	**0.62**
f_{n12}	210.58	210.66	0.04

3.2 Dynamic characteristics of the drive train

In this part, dynamic characteristics of the drive train are analyzed under different excitations of TVMS, WT, TS, WS and PMs. In addition, dynamic responses calculated by the proposed model and FE model are compared to further verify the reliability of the proposed model.

3.2.1 Effects of the time-varying mesh stiffness

Mesh stiffness of gear pair is the ability of the material to resist deformation when gears mesh. It varies with mesh positions and numbers of gear pair meshing. The frequency of TVMS is relative higher, which may be close to the natural frequencies of system. Therefore, TVMS is the one of the most important internal excitations of the healthy gear transmission system [37]. Lots of investigations have been conducted to calculate the TVMS, and the calculation methods of the TVMS of helical gear can be classified as [38]: empirical formula method, analytical method, FE method and analytical-FE method and so on. Considering the convenience and calculation precision, the empirical formula method is adopted in this paper based on Ref. [39], where TVMS is calculated by multiplying the mesh stiffness of the single sliced gear pair by the full length of contact line. The mesh stiffness of the single sliced gear pair can be obtained according to ISO 6336-1-2006 [40], and the length of contact line can be calculated based on Ref. [39].

The influence of mesh phase is significant on dynamic behaviors of the planetary gear [41]. According to calculation method of mesh phase proposed in Ref. [41], the relative phase between the *n*th sun-planet meshing and the arbitrarily chosen first sun-planet meshing is 0 in this paper. Similarly, the relative phase between the *n*th planet-ring meshing and the arbitrarily chosen first planet-ring meshing is also 0. Besides, the relative phase between the *n*th sun-planet and the *n*th ring-planet meshing is 0.5. As a result, the TVMS of the sun-planet gear pair, the planet-ring gear pair, the gear pair 1-2 and the gear pair 3-4 are calculated as shown in Fig. 5, in which solid lines mean the total gear mesh stiffness, and dash lines mean single gear pair mesh stiffness.

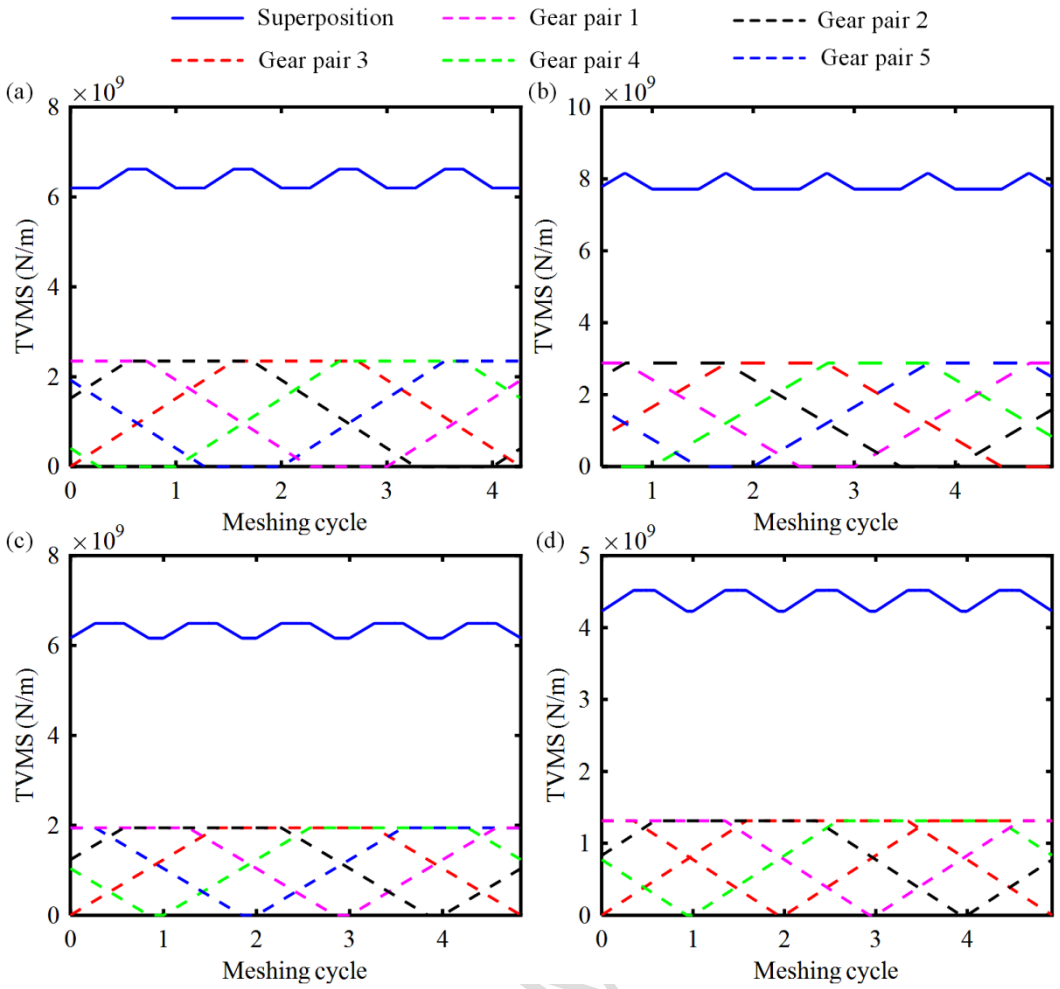

Fig. 5 TVMS of gear pairs: (a) sun-planet gear pair (b) planet-ring gear pair (c) gear pair 1-2 (d) gear pair 3-4

The vibration responses of gear 4 and sun gear in θ_z-direction based on the proposed model and FE model under the TVMS excitation are presented in Fig. 6. It depicts that the vibration responses obtained from the proposed model agree well with those obtained from the FE model.

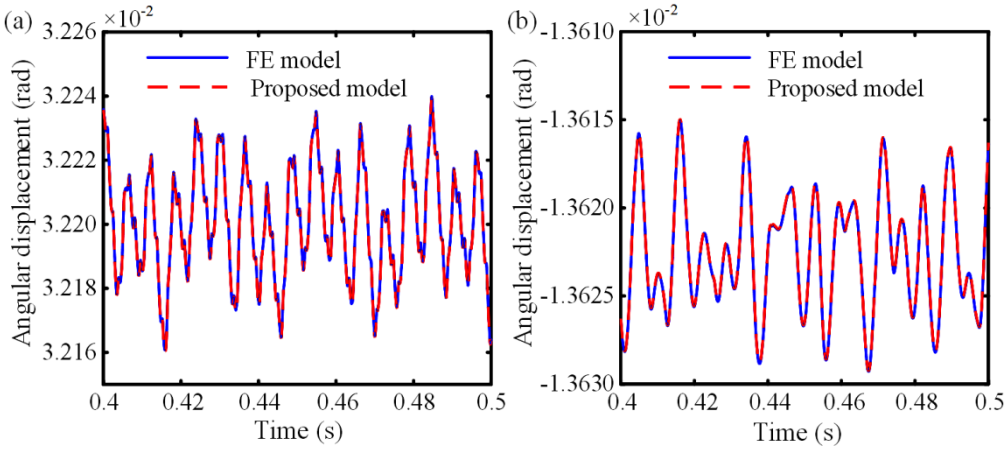

Fig. 6 Vibration responses of gear 4 and sun gear in θ_z-direction: (a) gear 4; (b) sun gear

Frequency spectrums of gears' vibration responses in θ_z-direction based on the proposed model at rated rotor

speed (17.2 r/min) are shown in Fig. 7. The mesh frequency of the gear pair 1-2 (f_{e12}=165.63 Hz) appears in all the frequency spectrums. Meanwhile, the amplitude at f_{e12} is relatively larger than others. Those are mainly because the gears can affect each other due to the coupling of gear meshing and f_{e12} is close to the first few natural frequencies.

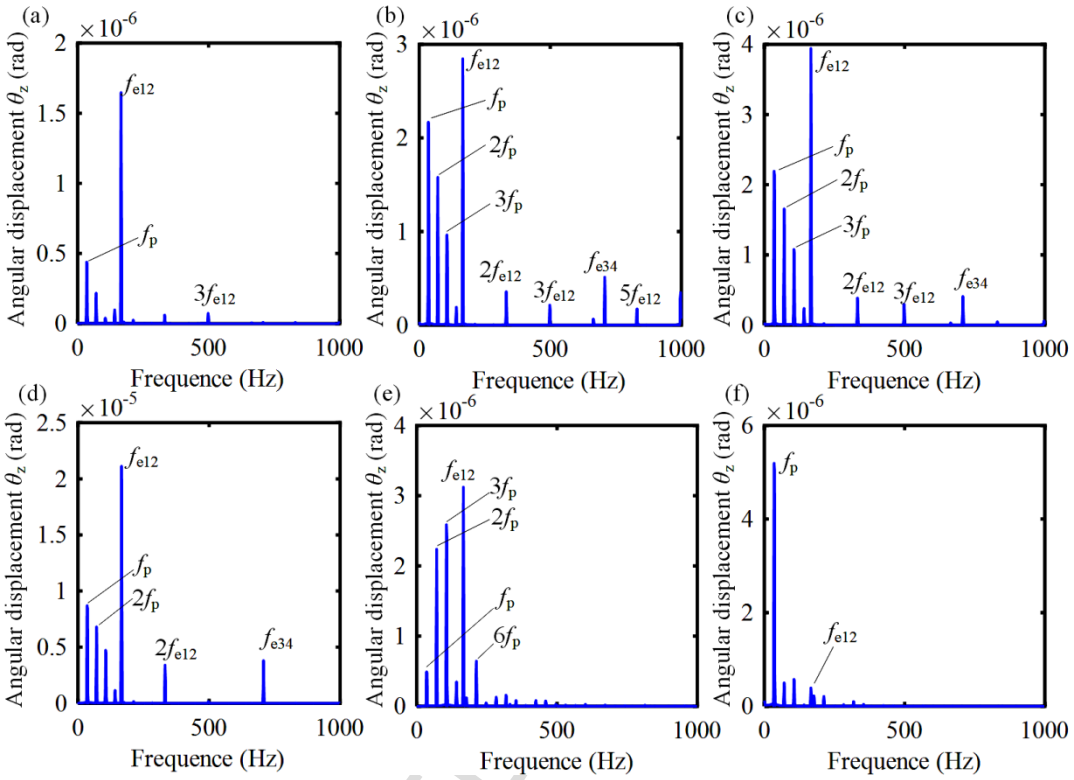

Fig. 7 Frequency spectrums of gears' vibration responses in θ_z-direction at rated rotor speed: (a) gear 1 (b) gear 2 (c) gear 3 (d) gear 4 (e) sun gear (f) planet gear

The amplitudes of vibration responses for gear 4 and sun gear in x-direction, y-direction and θ_z-direction under the TVMS excitation with different rotor speeds are shown in Fig. 8. It shows that the resonant peaks of the system appear when f_{e12} or $2f_{e12}$ is equal to the natural frequencies. This is mainly because the range of the mesh frequency of planetary gear, gear pairs 1-2 and 3-4 are f_p= 10.25 ~ 41 Hz, f_{e12}= 48.15 ~ 192.6 Hz and f_{e34}= 205.15 ~ 820.61 Hz, respectively. As a result, only the f_{e12} or $2f_{e12}$ is easier to cross with the first few natural frequencies (see Fig. 9). In addition, the intersection of the rated rotor speed and f_{e12} is far from the natural frequencies (see Fig. 9), and there are not the resonant peaks around the rated rotor speed (see Fig. 8). Therefore, the main shaft of wind turbine operating at the rated rotor speed can avoid the resonance vibration of system effectively.

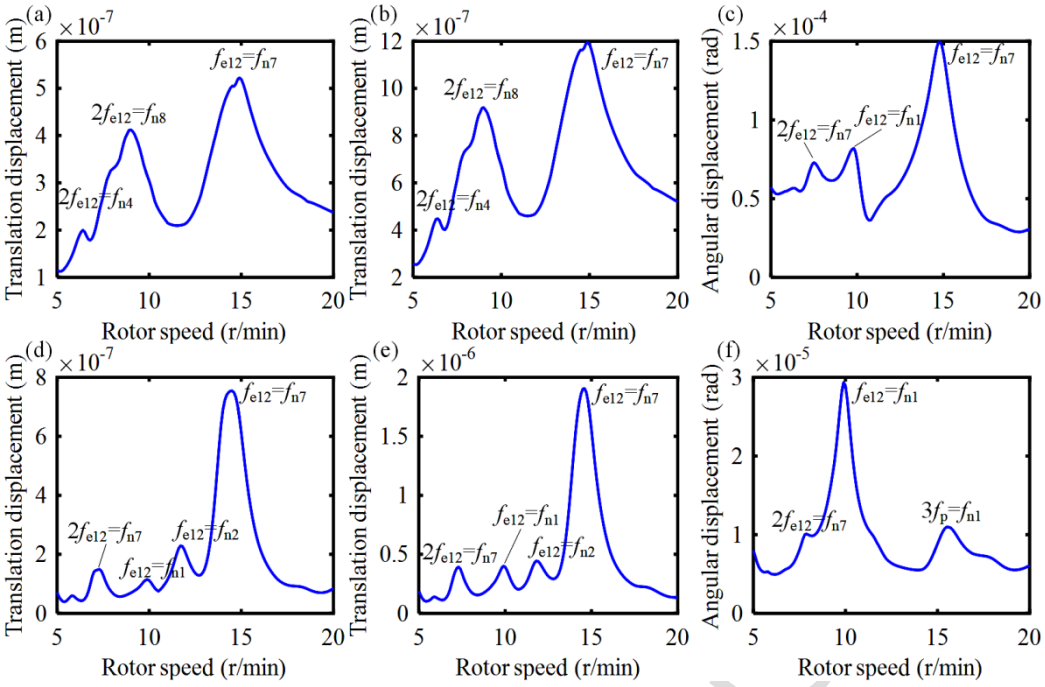

Fig. 8 Amplitudes of vibration responses for gear 4 and sun gear: (a) *x*-direction of gear 4 (b) *y*-direction of gear 4 (c) θ_z-direction of gear 4 (d) *x*-direction of sun gear (e) *y*-direction of sun gear (f) θ_z-direction of sun gear

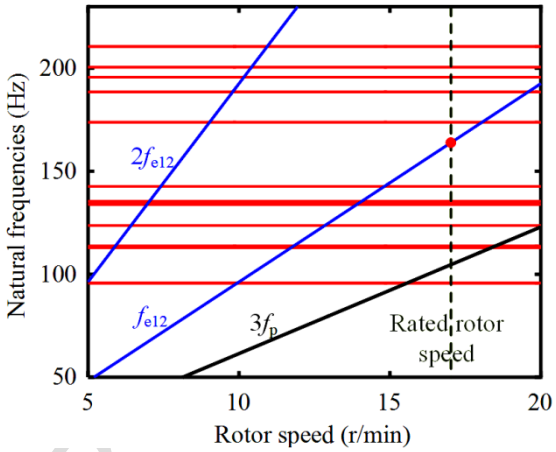

Fig. 9 Critical speed map of the system

3.2.2 Effects of the wind turbulence, tower shadow and wind shear

TS describes the reassignment of the wind speed due to the presence of the tower structure, while WS reflects the variation of wind speed with the vertical elevation. They can generate periodic fluctuations in aerodynamic loads [42, 43]. Except for these periodical processes, an operating wind turbine is also exposed to the stochastic excitations such as WT. The aerodynamic toque of the main shaft is altered significantly by these periodical and stochastic excitations. The variations of aerodynamic torque will be transferred into the dynamic responses of the drive train. In this section, the influences of the WT, TS, and WS on the dynamic characteristics

of wind turbine are discussed in detail.

WT is complex and random, but it can be modeled approximatively as the sum of harmonics according to Refs. [3, 44]:

$$v(t) = V_0(1 + \sum_{i=1}^{N} A_i \sin(\omega_i t)), \quad (14)$$

where V_0, A_i and ω_i are the mean wind speed, harmonic amplitude and frequency, respectively. The Dryden spectra is adopted to calculate A_i and the range of the harmonic frequencies are 0.1~10 Hz in this paper. The specification and power curve of a 1.5 WM fixed speed wind turbine are shown in Table 3 and Fig. 10, respectively.

Table 3 Specification of a 1.5WM wind turbine [43]

Notation	Parameter	Value
R (m)	Blade radius	36
H (m)	Hub height	80
a (m)	Tower radius	2
x (m)	Overhang	5
α	Wind shear component	0.1
n (r/min)	Rated rotor speed	17.2
Configuration	Blade number	3
V_{mean} (m/s)	Rated speed	15
V_{in} and V_{out} (m/s)	Cut-in and cut-out wind speeds	5, 20

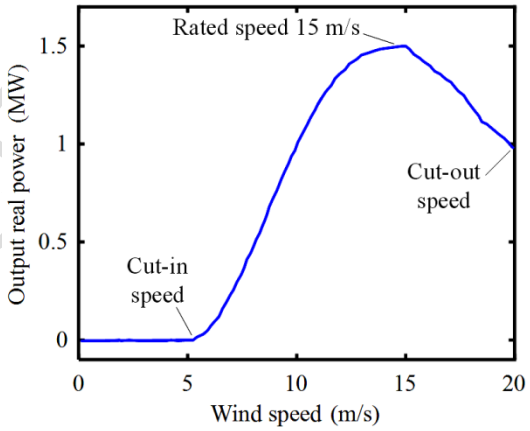

Fig. 10 Power curve of a 1.5 WM fixed speed wind turbine [43]

The wind speed variation calculated by the method proposed in Refs. [3, 44] is shown in Fig. 11a. Moreover, the variation of the aerodynamic torque due to the WT is shown in Fig. 11b, where the torque reaches the

maximum when the wind speed is equated to the rated speed. This is because the power of the wind turbine reaches the maximum at the rated wind speed for the fixed speed wind turbine (see Fig. 10).

In this paper, aerodynamic torques of a three bladed wind turbine considering the effects of the TS and WS are calculated according to the analytical formulation proposed by Dolan et. al in Ref. [42, 43], which is concise and effective. In order to make this paper self-contained, a brief introduction of main equations is provided. The "equivalent wind speed method" is adopted to represent the actual spatially varying wind speed, which is a wind speed without radial dependence. The final expressions for equivalent wind speed due to wind shear ($v_{eq_{ws}}$) and tower shadow ($v_{eq_{ts}}$) are shown in Eqs. (15) and (16), respectively.

$$v_{eq_{ws}} = V_h\left(\frac{\alpha(\alpha-1)}{8}\left(\frac{R}{H}\right)^2 + \frac{\alpha(\alpha-1)(\alpha-2)}{60}\left(\frac{R}{H}\right)^3 \cos(3\theta_b)\right), \tag{15}$$

$$v_{eq_{ts}} = \frac{V_h}{3R^2}\sum_{b=1}^{3}\left(\frac{a^2}{\sin^2\theta_b}\ln\left(\frac{R^2\sin^2\theta_b}{x^2}+1\right) - \frac{2a^2R^2}{R^2\sin^2\theta_b + x^2}\right), \tag{16}$$

where V_h, R, H, α, θ_b, a denote the hub height wind speed, blade radius, hub height, wind shear component, azimuthal angle of the blade and tower radius, respectively. The aerodynamic torque (T_{areo}) can be calculated according to Eq. (17), in which the first term is the torque due to stead wind and second term is the disturbance in torque due to wind shear and tower shadow.

$$T_{aero} = \frac{1}{2}\frac{\rho A V_h^3 C_p}{w_{rotor}} + \frac{\rho A V_h C_p R}{\lambda_0}\left(v_{eq_{ws}} + v_{eq_{ts}}\right), \tag{17}$$

where ρ, A, C_p, ω_{rotor}, λ_0 denote the air density, cross-sectional area of rotor, rotor power coefficient, rotor angular velocity and tip-speed ratio.

The torque variations due to TS and WS are calculated and shown in Fig. 11c. It is shown that the torque variation under the effect of TS is distinct; however, the influence of WS is relatively negligible. In addition, the aerodynamic torque under the comprehensive effects of WT, TS and WS is shown in Figs. 11d, in which a remarkable reduction appears around 90s. This is because at this moment the reductions of torque due to WT and TS happen to be superposed.

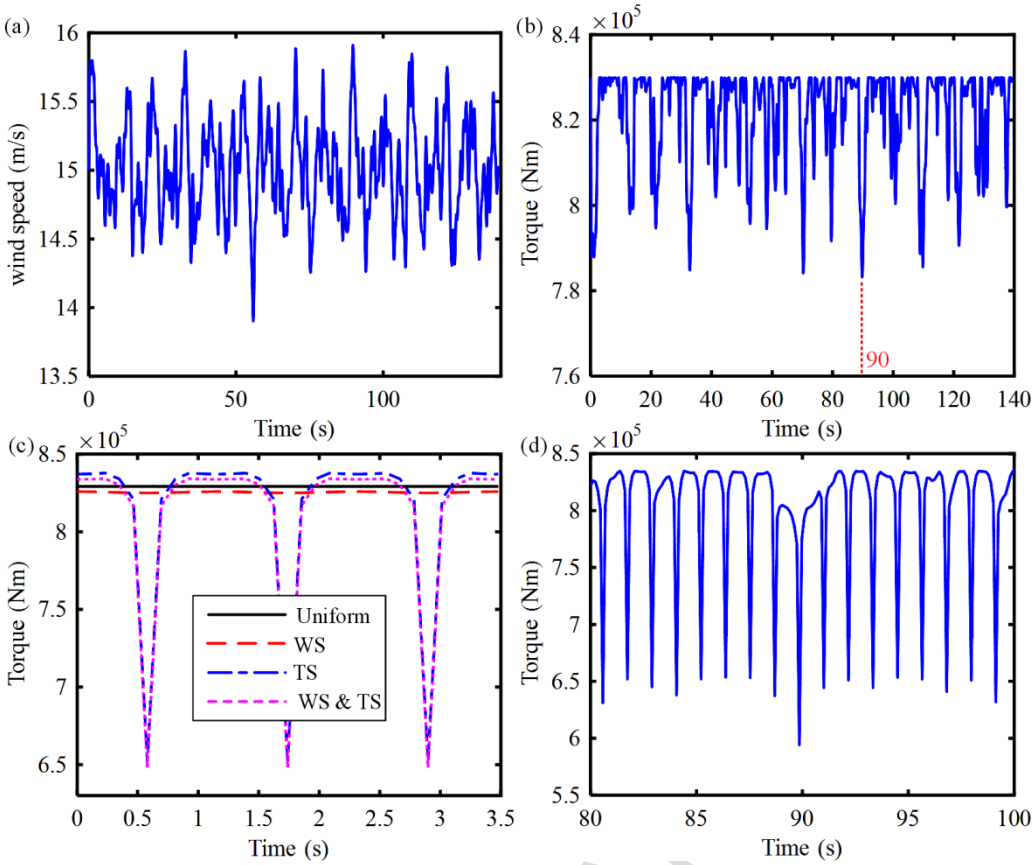

Fig. 11 Wind speed variation and torque variations under WT, WS and TS: (a) wind speed variation under WT (b) torque under WT (c) torque under WS, TS, WS&TS or uniform wind speed (d) torque under WT, TS and WS

The vibration responses and frequency spectrums of gear 4 in θ_z-direction under the WT, TS, WS and comprehensive effects (including WT, TS and WS) are shown in Figs. 12 and 13, which reveal the following phenomena:

(1) The vibration amplitude of gear 4 in θ_z-direction under TS excitation is larger than that under the excitations of WT and WS, which indicates that TS is the most significant excitation source for the drive train compared with WT and WS (see Figs. 12a, 12b and 12c). Besides, Fig. 11d and Fig. 12d present similar variation trends. This is because the angular displacement can directly reflect the variations of torque. Therefore, the angular displacement of gear 4 in θ_z-direction also has a notable reduction around 90s. This will introduce a remarkable fluctuation to output power of wind turbine.

(2) As shown in Figs. 13b and 13c, the frequency spectrum of gear 4 in θ_z-direction under WS only includes the $3f_n$ (i.e., the tripling of rotation frequency of the main shaft), whereas $3nf_n$ (n=1, 2, 3…) appears under TS. This is because the aerodynamic torque under WS is a sinusoidal function. However, TS is generally assumed to affect

the wind speed at the bottom half of the blade operating region, which makes the torque under TS more complex.

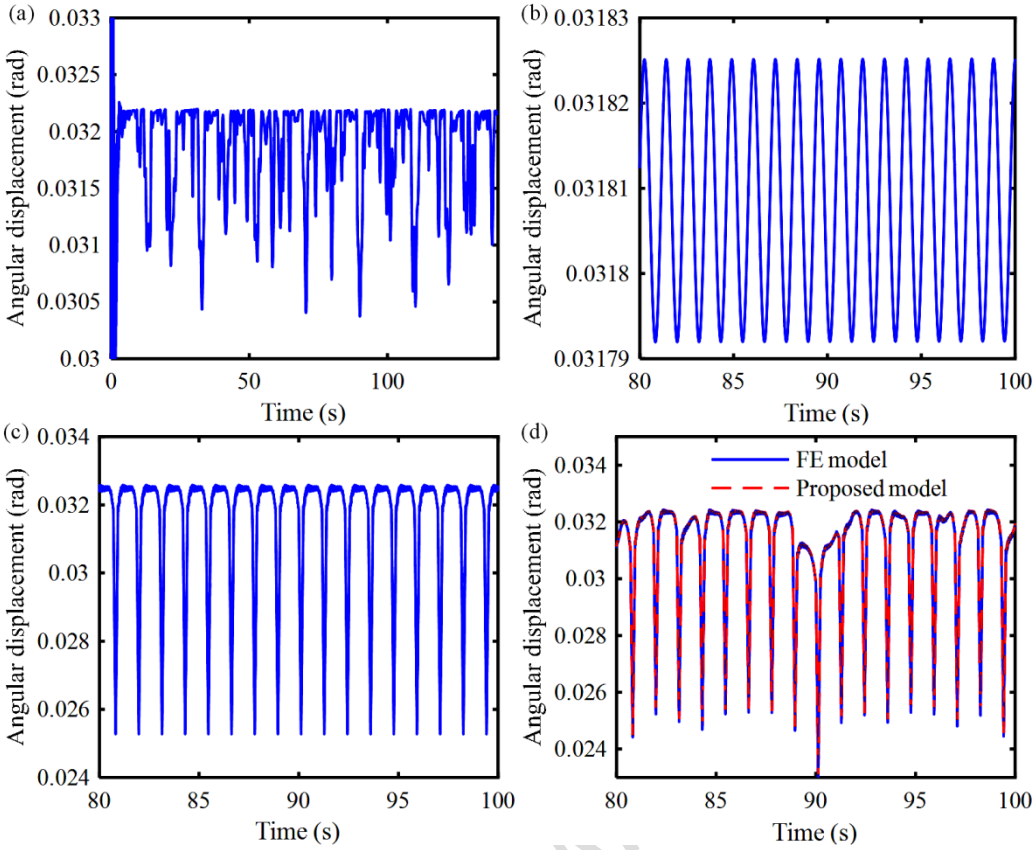

Fig. 12 Vibration responses of gear 4 in θ_z-direction under different excitations: (a) WT (b) WS (c) TS (d) WS, TS and WT

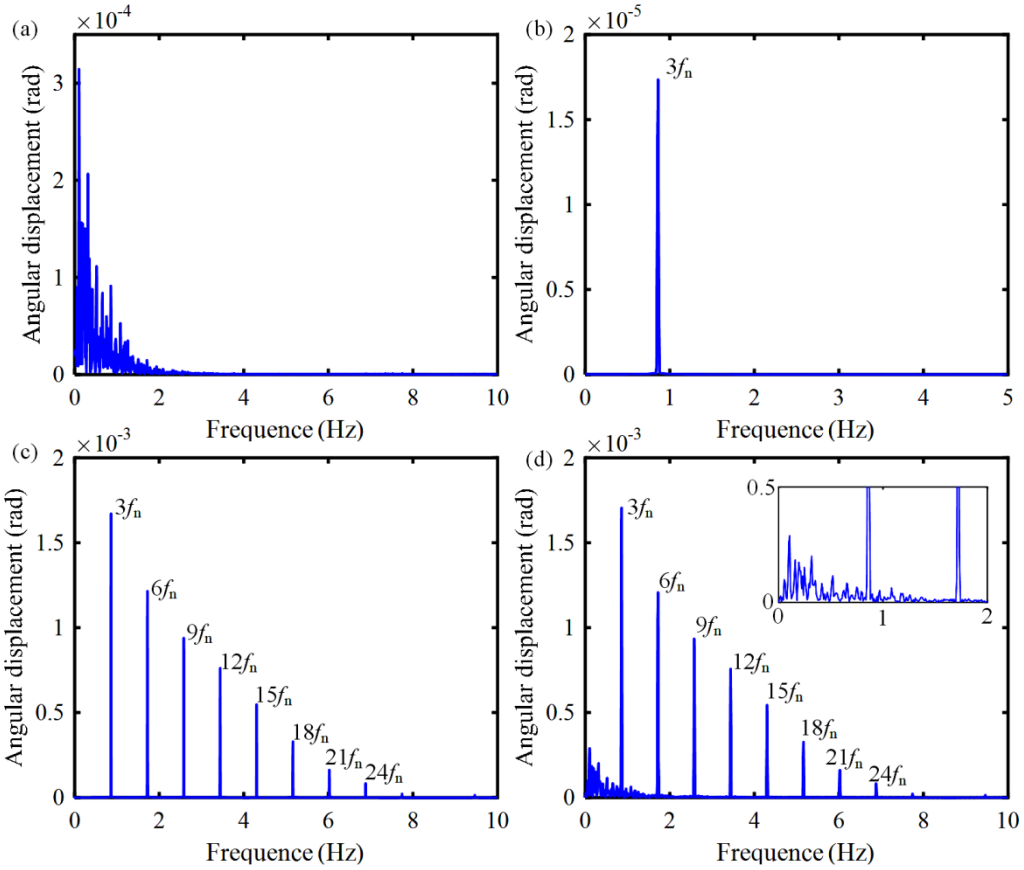

Fig. 13 Frequency spectrums of gear 4 in θ_z-direction under different excitations: (a) WT (b) WS (c) TS (d) WS, TS and WT

(3) Vibration responses of gear 4 in θ_z-direction under the comprehensive effects based on proposed model and FE model agree well (see Fig. 12d), which further proves the reliability of the proposed model. In addition, comparing with Fig. 13c and Fig. 13d, it can be found that the $3f_n$ effect is more remarkable under the accumulation of WT, TS and WS.

3.2.3 Effects of platform motions

Compared with the bottom-fixed wind turbine, the OFWT has an extra excitation generated by PMs. Prior investigations have pointed out that the platform pitch and surge motions markedly impact the aerodynamic torque of an OFWT[45, 46]. Therefore, it is anticipated that the dynamic characteristics of the drive train system will also be significantly influenced by platform pitch and surge motions. In addition, the effect of platform heave motion is also discussed in this paper. To simplify the analysis, the pitch, surge and heave motions are assumed to be sinusoidal fluctuation: $x = A\cos(2\pi ft)$ with $A_{\text{pitch}} = 2°$, $f_{\text{pitch}} = 0.1$ Hz for pitch case, $A_{\text{surge}} = 2$ m, $f_{\text{surge}} = 0.1$ Hz for the surge case and $A_{\text{heave}} = 0.3$ m, $f_{\text{heave}} = 0.1$ Hz for heave case. These oscillation parameters are carefully chosen to meet the actual situation that a full-scaled operating OFWT is likely to experience [47-49]. The relative wind speed of the wind turbine (superposition of the free-stream wind velocity and the velocity induced by platform motions) under the platform pitch and surge motions are written as follow [45, 46]:

$$v_{\text{relative}}(t) = \begin{cases} v(t) + A_{\text{pitch}}/180 \times \pi \times H \times 2\pi f_{\text{pitch}} \sin(2\pi f_{\text{pitch}} \times t) & \text{Pitch motion} \\ v(t) + A_{\text{surge}} \times 2\pi f_{\text{surge}} \sin(2\pi f_{\text{surge}} \times t) & \text{Surge motion} \end{cases}, \tag{18}$$

where $v(t)$ is the free-stream wind velocity. Aerodynamic torque variations under the platform pitch and surge motions are shown in Fig. 14. In these cases, the WT, TS and WS are all excluded to focus on the influences of the PMs. It is worth noting that the motion amplitude of the platform heave motion is much smaller than the hub height, therefore the effect of the platform heave motion on WS is negligible. Therefore, the platform heave motion only generates the base excitation on the drive train.

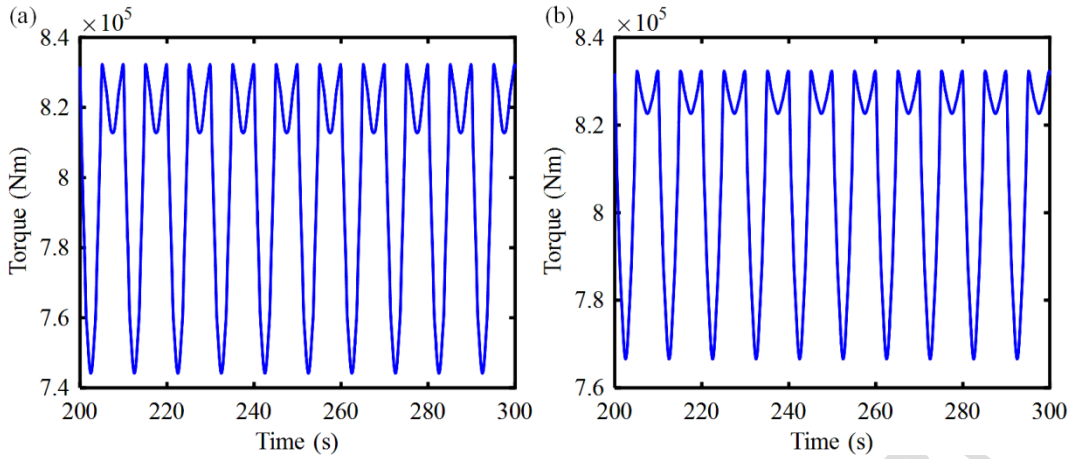

Fig. 14 Aerodynamic torque variations under the platform pitch and surge motions: (a) pitch motion; (b) surge motion

Based on the proposed model and FE model, vibration responses of gear 4 in θ_z-direction under different platform motions are shown in Fig. 15. It is shown that great agreement is reached between both models, which further validate the reliability of the proposed flexible dynamic model. The frequency spectrum of gear 4 in θ_z-direction under different platform motions are shown in Fig. 16. It is observed that vibration amplitudes of gear4 in θ_z-direction under the excitations of platform pitch and surge motions are bigger than those under the excitation of platform heave motion. This is because the platform pitch and surge motions not only generate the base excitation on the drive train but also have marked influences on the relative wind speed of wind turbine (see Eq. 14). In addition, the frequency spectrum of gear 4 in θ_z-direction under the excitation of platform heave motion only includes the excitation frequency. As for the pitch and surge cases, however, higher harmonics of the excitation frequency are also clear observed.

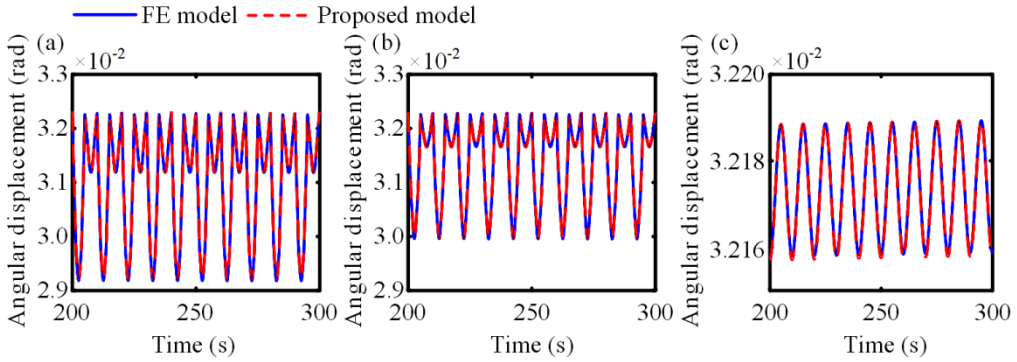

Fig. 15 Vibration responses of gear 4 in θ_z-direction under different excitations of PMs: (a) pitch; (b) surge; (c) heave

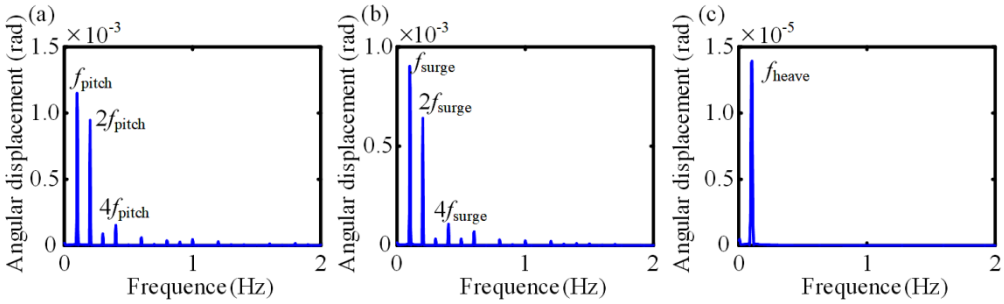

Fig. 16 Frequency spectrum of gear 4 in θ_z-direction under different excitations of PMs: (a) pitch; (b) surge; (c) heave

Vibration amplitudes of gears under the platform heave motion at rated rotor speed are listed in Table 4. The amplitudes in the θ_x- and θ_z-direction are relatively bigger than other directions for two parallel shaft gears (gear 1, gear 2, gear 3 and gear 4). The amplitudes of planetary gear (sun gear, planet 1, planet 2 and planet 3) is more dominant than those of parallel shaft gears. Those denote that the effect of platform heave motion in the θ_x- and θ_z-direction is bigger than other directions. In addition, the effect of platform heave motion on the planetary gear is bigger than parallel shaft gears. Therefore, only the base excitation also has a noteworthy influence on the vibration of gear shafts in the rotation direction (i.e., θ_z-direction), which has a direct influence on the power fluctuation of wind turbine.

Table 4 Vibration amplitudes of gears under the platform heave motion at rated rotor speed

Gears	x (m)	y (m)	z (m)	θ_x (rad)	θ_y (rad)	θ_z (rad)	Gears	x (m)	y (m)	z (m)	θ_x (rad)	θ_y (rad)	θ_z (rad)
Gear 1	5.80e-8	0.3	1.48e-12	2.34e-6	5.15e-8	1.84e-6	Sun gear	1.31e-6	0.3	1.19e-12	1.176e-5	2.86e-6	1.84e-6
Gear 2	1.82e-12	0.3	1.89e-12	1.48e-6	2.87e-12	5.81e-6	Planet 1	1.60e-7	0.3	9.54e-8	3.15e-6	2.03e-6	2.09e-5
Gear 3	8.67e-13	0.3	1.81e-12	1.15e-6	4.67e-12	5.81e-6	Planet 2	3.76e-8	0.3	2.31e-6	2.81e-6	8.87e-7	1.05e-5
Gear 4	5.34e-13	0.3	1.48e-13	1.07e-6	1.90e-12	1.40e-5	Planet 3	6.06e-7	0.3	2.40e-6	3.97e-6	1.17e-6	1.25e-5

3.2.4 Effects of the combined excitations

The vibration responses of gear 4 in θ_z-direction under the combined excitations (including TVMS, WT, TS, WS and PMs) obtained from proposed model and FE model are shown in Fig. 17a, which strengthens the reliability of the proposed model once again. The frequency spectrum of gear 4 in θ_z-direction based on the proposed model is shown in Fig. 17b. The vibration amplitude at 0.1 Hz is the largest, which can be accounted for by the excitation frequencies of PMs are all 0.1 Hz and WT has an additional contribution to 0.1 Hz. This is to say that the combined effects of PMs and WT is bigger than the effect of TS on the vibration response of gear 4 in θ_z-

direction in this paper. In addition, mesh frequencies of gear pairs can be found in the frequency spectrum, but the amplitude is comparatively small.

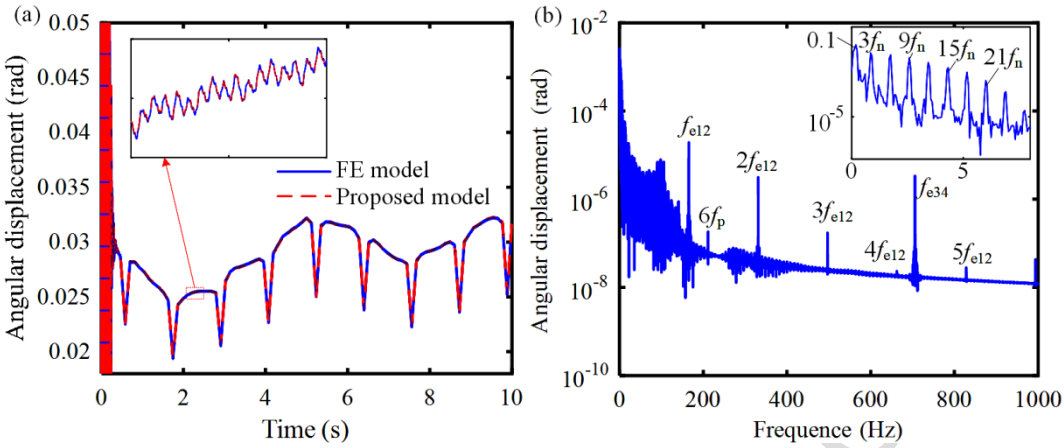

Fig. 17 Vibration response and frequency spectrum of gear 4 in θ_z-direction: (a) vibration response (b) frequency spectrum

From the Fig. 7d, Fig. 13, Fig. 16 and Table 4, we can easily get the vibration amplitudes of gear 4 in θ_z-direction under TVMS, WT, TS, WS, platform pitch motion, platform surge motion and platform heave motion. A directly comparisons are summarized in the Table 5. It is found that the amplitude under the TS excitation is the biggest, followed by platform pitch motion, platform surge motion and WT. This indicates that the TS is the most significant excitation source for OFWT drive train analyzed in this paper, followed by platform pitch motion, platform surge motion and WT.

Table 5 The comparison of the vibration amplitudes of gear 4 under various excitations

	Internal excitation	Wind variation			Platform motions		
Excitation	TVMS	WT	WS	TS	Pitch	Surge	Heave
Vibration amplitudes (×e-5 rad)	2	31	1.8	170	120	90	1.4

4. Conclusions

In this paper, a flexible dynamic model is proposed to investigate the dynamic characteristics of the drive train for an Offshore Floating Wind Turbine (OFWT). This model includes the flexibilities of the planet carrier and ring gear. Comparisons with the finite element model established in ANSYS show that the proposed model is

reliable enough to capture the dynamic characteristics of the OFWT drive train. Afterwards, the influences of Time-varying Mesh Stiffness (TVMS), Wind Turbulence (WT), Tower Shadow (TS), Wind Shear (WS) and Platform Motions (PMs) on the dynamic characteristics of the drive train are studied in detail one by one. Based on the simulation and discussion, the following conclusions are drawn:

(1) Gears can affect each other due to the coupling of gear meshing. The resonant peaks of the system are more likely to appear when the mesh frequency or its multiplication of the gear pair 1-2 is equal to the natural frequencies under the TVMS excitation.

(2) The frequency spectrum of gear 4 in θ_z-direction under WS only includes the $3f_n$ (i.e., the tripling of rotation frequency for the main shaft), whereas $3nf_n$ (n=1, 2, 3…) appears under TS.

(3) The vibration amplitudes of gear 4 in θ_z-direction under the platform pitch and surge motions are bigger than platform heave motion. Moreover, the frequency spectrum under the excitation of platform heave motion only includes the excitation frequency. Under the platform pitch and surge motions, however, additional higher harmonics are also observed.

(4) By comparing the vibration amplitudes of gear 4 in θ_z-direction, TS is found to be the most significant excitation source for the OFWT drive train analyzed in this paper, followed by platform pitch motion, platform surge motion and WT.

Acknowledgment

This work is supported by the National Natural Science Foundation of China (Grant No.11632011).

Appendix:

Nomenclature

$\boldsymbol{C}$	Damping matrix of the system

$\boldsymbol{C}_{ij}$	Damping matrix of the gear pair *ij*
$\boldsymbol{D}$	The material property matrix
$\boldsymbol{F}_{\boldsymbol{u}}$	External force vector of the system
$\boldsymbol{K}$	Stiffness matrix of the system
$\boldsymbol{K}_{ij}$	Mesh stiffness matrix of the gear pair *ij*
$\boldsymbol{M}$	Mass matrix of the system
$\boldsymbol{M}_{ij}$	Mass matrix of the gear pair *ij*
$\boldsymbol{V}_{3i}^{k}$	The unit vector at node *k*
$\boldsymbol{V}_{1i}^{k}$, $\boldsymbol{V}_{2i}^{k}$	Unit vectors along the reference surface
$\boldsymbol{X}_{ij}$	Displacement vector matrix of the gear pair *ij*
a	Tower radius
A	Cross-sectional area of rotor
A_i	Harmonic amplitude of wind turbulence
C_p	rotor power coefficient
$e_{ij}(t)$	Static transmission error
f_{e12}	Mesh frequency of gear pair 1-2
f_{e34}	Mesh frequency of gear pair 3-4
f_{p}	Mesh frequency of the planet gear
f_{n}	The rotation frequency of main shaft
$H^k(\zeta)$	One-dimensional function in ζ-direction
H	Hub height
k_{ij}	The time-varying mesh stiffness of the helical gear pair *ij*
$N^k(\xi, \eta)$	The shape function of the shell in the middle surface
O_i, O_j	Geometrical centers of the gears *i* and *j*
$p_{exter}(t)$	Relative displacement of the external gear meshing
R	Blade radius
T_{areo}	Aerodynamic torque
r_{bi}, r_{bj}	Radii of base circles of gear *i* and *j*
u_i^k	The nodal displacement at node *k*

$v(t)$	Wind speed of the wind turbulence
V_0	Mean wind speed
V_h	Hub height wind speed
$x_i, x_j, y_i, y_j, z_i, z_j$	Displacements in three translation directions of gear i and gear j
x_i^k	Position vectors of the nodes

1

2 Greek symbols

α	Wind shear component
α_{ij}	The relative position angle between the connecting line of gear centers and the positive x-axis of gear i
ω_i	Harmonic frequency of wind turbulence
ω_{rotor}	rotor angular velocity
φ_{ij}	The operating pressure angle of the helical gear
ψ_{ij}	The angle between the plane of action and positive y-axis
θ_b	Azimuthal angle of the blade
$\theta_{xi}, \theta_{xj}, \theta_{yi}, \theta_{yj}, \theta_{zi}, \theta_{zj}$	Displacements in three rotation directions of gear i and gear j
θ_1^k, θ_2^k	Rotational degrees of freedom along the unit vector
λ_0	Tip-speed ratio
ρ	Air density

3

4 Abbreviations

CMS	Component Mode Synthesis
FE	Finite Element
OFWT	Offshore Floating Wind Turbine
TS	Tower Shadow
TVMS	Time-varying Mesh Stiffness
WS	Wind Shear
WT	Wind Turbulence

5

6 # References

[1] Han Q, Wei J, Han Q, Zhang H. Dynamics and vibration analyses of gearbox in wind turbine: Springer, 2017.

[2] Hu W. Advanced wind turbine technology: Springer, 2018.

[3] Abo-Khalil AG, Lee DC. Dynamic modeling and control of wind turbines for grid-connected wind generation system. In: 37th IEEE Power Electronics Specialists Conference, Jeju, Korea. 2006; 1-6.

[4] Wei S, Zhao J, Han Q, Chu F. Dynamic response analysis on torsional vibrations of wind turbine geared transmission system with uncertainty. Renewable Energy. 2015;78:60-7.

[5] Gu B, Liu Y, Xu Q, Kang S. Research cage wind turbines' dynamic characteristics based on time-varying parameters. International Journal of Control and Automation. 2014;7(10):155-66.

[6] Shi W, Kim C-W, Chung C-W, Park H-C. Dynamic modeling and analysis of a wind turbine drivetrain using the torsional dynamic model. International Journal of Precision Engineering and Manufacturing. 2012;14(1):153-9.

[7] Zhao M, Ji JC. Nonlinear torsional vibrations of a wind turbine gearbox. Applied Mathematical Modelling. 2015;39(16):4928-50.

[8] Guo Y, Parker RG. Dynamic modeling and analysis of a spur planetary gear involving tooth wedging and bearing clearance nonlinearity. European Journal of Mechanics - A/Solids. 2010;29(6):1022-33.

[9] Guo Y, Keller J, Parker RG. Nonlinear dynamics and stability of wind turbine planetary gear sets under gravity effects. European Journal of Mechanics - A/Solids. 2014;47:45-57.

[10] Shi W, Park H-C, Na S, Song J, Ma S, Kim C-W. Dynamic analysis of three-dimensional drivetrain system of wind turbine. International Journal of Precision Engineering and Manufacturing. 2014;15(7):1351-7.

[11] Srikanth P, Sekhar AS. Dynamic analysis of wind turbine drive train subjected to nonstationary wind load excitation. Proceedings of the Institution of Mechanical Engineers, Part C: Journal of Mechanical Engineering Science. 2014;229(3):429-46.

[12] Srikanth P, Sekhar AS. Wind turbine drive train dynamic characterization using vibration and torque signals. Mechanism and Machine Theory. 2016;98:2-20.

[13] Qin D, Wang J, Lim TC. Flexible multibody dynamic modeling of a horizontal wind turbine drivetrain system. Journal of Mechanical Design. 2009;131(11):114501.

[14] Yi P, Zhang C, Guo L, Shi T. Dynamic modeling and analysis of load sharing characteristics of wind turbine gearbox. Advances in Mechanical Engineering. 2015;7(3):1687814015575960.

[15] Zhao M, Ji J. Dynamic Analysis of Wind Turbine Gearbox Components. Energies. 2016;9(2):110.

[16] Zhai H, Zhu C, Song C, Liu H, Bai H. Influences of carrier assembly errors on the dynamic characteristics for wind turbine gearbox. Mechanism and Machine Theory. 2016;103:138-47.

[17] Zhu C, Xu X, Liu H, Luo T, Zhai H. Research on dynamical characteristics of wind turbine gearboxes with flexible pins. Renewable Energy. 2014;68:724-32.

[18] Li Y, Castro AM, Martin JE, Sinokrot T, Prescott W, Carrica PM. Coupled computational fluid dynamics/multibody dynamics method for wind turbine aero-servo-elastic simulation including drivetrain dynamics. Renewable Energy. 2017;101:1037-51.

[19] Nejad AR, Guo Y, Gao Z, Moan T. Development of a 5 MW reference gearbox for offshore wind turbines. Wind Energy. 2016;19(6):1089-106.

[20] Nejad AR, Bachynski EE, Li L, Moan T. Correlation between Acceleration and Drivetrain Load Effects for Monopile Offshore Wind Turbines. Energy Procedia. 2016;94:487-96.

[21] Helsen J, Peeters P, Vanslambrouck K, Vanhollebeke F, Desmet W. The dynamic behavior induced by different wind turbine gearbox suspension methods assessed by means of the flexible multibody technique. Renewable Energy. 2014;69:336-46.

[22] Guo Y, Keller J, Lacava W. Combined effects of gravity, bending moment, bearing clearance, and Input torque on wind turbine planetary gear load sharing: preprint. American Gear Manufacturers Association Fall Technical Meeting, Dearborn, MI, Oct, 2012; 28-30.

[23] Wang S, Zhu C, Song C, Han H. Effects of elastic support on the dynamic behaviors of the wind turbine drive

train. Frontiers of Mechanical Engineering. 2017;12(3):348-56.

[24] Zhu C, Chen S, Liu H, Huang H, Li G, Ma F. Dynamic analysis of the drive train of a wind turbine based upon the measured load spectrum. Journal of Mechanical Science and Technology. 2014;28(6):2033-40.

[25] Zhu C, Chen S, Song C, Liu H, Bai H, Ma F. Dynamic analysis of a megawatt wind turbine drive train. Journal of Mechanical Science and Technology. 2015;29(5):1913-9.

[26] Xing Y, Karimirad M, Moan T. Effect of spar-type floating wind turbine nacelle motion on drivetrain dynamics. Conference Effect of spar-type floating wind turbine nacelle motion on drivetrain dynamics, Copenhagen, Denmark.

[27] Kahraman A, Kharazi AA, Umrani M. A deformable body dynamic analysis of planetary gears with thin rims. Journal of Sound and Vibration. 2003;262(3):752-68.

[28] Chen Z, Shao Y. Mesh stiffness of an internal spur gear pair with ring gear rim deformation. Mechanism and Machine Theory. 2013;69:1-12.

[29] Peeters JLM, Vandepitte D, Sas P. Analysis of internal drive train dynamics in a wind turbine. Wind Energy. 2006;9(1-2):141-61.

[30] Helsen J, Vanhollebeke F, Marrant B, Vandepitte D, Desmet W. Multibody modelling of varying complexity for modal behaviour analysis of wind turbine gearboxes. Renewable Energy. 2011;36(11):3098-113.

[31] Jin X, Li L, Ju W, Zhang Z, Yang X. Multibody modeling of varying complexity for dynamic analysis of large-scale wind turbines. Renewable Energy. 2016;90:336-51.

[32] Wang Q, Li Z, Ma H, Wen B. Effects of different coupling models of a helical gear system on vibration characteristics. Journal of Mechanical Science and Technology. 2017;31(5):2143-54.

[33] Zhang Y, Wang Q, Ma H, Huang J, Zhao C. Dynamic analysis of three-dimensional helical geared rotor system with geometric eccentricity. Journal of Mechanical Science and Technology. 2013;27(11):3231-42.

[34] Wei J, Zhang A, Qin D, Lim TC, Shu R, Lin X, et al. A coupling dynamics analysis method for a multistage

planetary gear system. Mechanism and Machine Theory. 2017;110:27-49.

[35] Kwon YW, Bang H. The finite element method using MATLAB (2nd ed.). Boca Raton, FL: CRC Press, 2015.

[36] Craig R, Bampton M. Coupling of substructures for dynamic analyses. AIAA journal. 1968;6(7):1313-9.

[37] Chen Z, Shao Y, Su D. Dynamic simulation of planetary gear set with flexible spur ring gear. Journal of Sound and Vibration. 2013;332(26):7191-204.

[38] Feng M, Ma H, Li Z, Wang Q, Wen B. An improved analytical method for calculating time-varying mesh stiffness of helical gears. Meccanica. 2017;53(4-5):1131-45.

[39] Zhu CC, Lu B, Song CS, Qin DT. Dynamic analysis of a heavy duty marine gearbox with gear mesh coupling. Proceedings of the Institution of Mechanical Engineers, Part C: Journal of Mechanical Engineering Science. 2009;223(11):2531-47.

[40] ISO/CD 6336-1, Calculation of load capacity of spur and helical gears—part1: Basic principles, introduction and general influence factors, International Organization for Standardizations. Geneva, Switzerland, 2006.

[41] Parker RG, Lin J. Mesh Phasing Relationships in Planetary and Epicyclic Gears. Journal of Mechanical Design. 2004;126(2):525-34.

[42] Dolan DSL, Lehn PW. Simulation model of wind turbine 3p torque oscillations due to wind shear and tower shadow. IEEE Transactions on Energy Conversion. 2006;21(3):717-24.

[43] Das S, Karnik N, Santoso S. Time-domain modeling of tower shadow and wind shear in wind turbines. ISRN Renewable Energy. 2011;2011:1-11.

[44] Nichita C, Luca D, Dakyo B, Ceanga E. Large band simulation of the wind speed for real time wind turbine simulators. IEEE Transactions on Energy Conversion. 2002;17(4):523-9.

[45] Wen B, Dong X, Tian X, Peng Z, Zhang W, Wei K. The power performance of an offshore floating wind turbine in platform pitching motion. Energy. 2018;154:508-21.

[46] Wen B, Tian X, Dong X, Peng Z, Zhang W. Influences of surge motion on the power and thrust characteristics of

an offshore floating wind turbine. Energy. 2017;141:2054-68.

[47] Jonkman J. Influence of Control on the Pitch Damping of a Floating Wind Turbine. 46th AIAA Aerospace Sciences Meeting and Exhibit, Reno, Nevada. 2008; 1306.

[48] Goupee AJ, Koo BJ, Kimball RW, Lambrakos KF, Dagher HJ. Experimental comparison of three floating wind turbine concepts. Journal of Offshore Mechanics and Arctic Engineering. 2014;136(2):020906-1.

[49] Sebastian T, Lackner M. Analysis of the induction and wake evolution of an offshore floating wind turbine. Energies. 2012;5(4):968-1000.

Highlights

- A flexible dynamic model of the drive train is established.
- Flexibilities of the planet carrier, ring gear and gear shafts are considered.
- The flexible model is verified by a finite element model.
- Dynamic characteristics of the drive train under different excitations are studied.